Stress analysis of brittle spheres under multiaxial loading

M.K. Gundepudi [a], B.V. Sankar [a,b,*], J.J. Mecholsky, Jr. [b,c], D.C. Clupper [c]

[a] *Department of Aerospace Engineering, Mechanics and Engineering Science, University of Florida, Gainesville, FL 32611-6250, USA*
[b] *Engineering Research Center for Particle Science and Technology, University of Florida, Gainesville, FL 32611-6135, USA*
[c] *Department of Materials Science and Engineering, University of Florida, Gainesville, FL 32611-6400, USA*

Abstract

An analytical method has been developed to determine the state of three-dimensional stresses in a sphere subjected to multiple contact loads. The method has been used to study the stress distribution in a sphere under a variety of loading conditions important to particulate systems. It is found that in the case of three-point in-plane loading the maximum tensile stresses are larger than that in uniaxial compression. As the number of contact points increases, the maximum internal tensile stress, in general, decreases as the state of stress inside the sphere approaches hydrostatic compression. The method was used to analyze the stresses in some tests carried out on glass and alumina spheres. The stress analysis indicates that the maximum contact stress and hence the tensile stress outside the contact circle correlate well with failure and are partially responsible for attrition in particulate systems. © 1997 Elsevier Science S.A.

Keywords: Attrition; Failure; Contact mechanics; Brittle spheres; Stress analysis

1. Introduction

Attrition is the wear and fracture of particles during transport and handling. Some of the industries which face this problem are the cement, agricultural, mineral and chemical industries. Attrition is manifested in many ways, including formation of fine dust, breakage of bigger particles into smaller ones, contamination of food grains, etc. The effect of attrition is more widespread and is not understood properly because of the complex nature of the process itself. In real time flow systems, the shape, size and number of particles are highly irregular and change with time. Attrition depends on particle shape and size, the fluid or gas velocity, and the material properties of the particles, like Young's modulus and fracture toughness. In fact, attrition occurs whenever there is some relative velocity between particles in contact. It occurs during collision between particles or when the particles collide against the wall of the container or during confined compression. Hence, the number of particles change with time and it is very difficult to simulate such a granular flow. In order to understand the physical process involved in attrition and to assess attrition, a number of tests have been conducted by different people. A detailed analysis of attrition and the various tests to describe it were studied by Bemrose and Bridgewater [1] in 1987. They discussed the process of

attrition, the different types of attrition and the industries affected due to attrition. It is very important to get the complete stress distribution of an attriting particle for a better understanding of its resistance to attrition. One of the important steps in this understanding is the analysis of the single particle in detail under different types of loading. The particle under uniaxial compression was studied in detail by Shipway and Hutchings [2] but they did not discuss the state of internal stress under such a loading. Kienzler and Schmitt [3] studied the compression of spheres using the finite element method (FEM). However, they did not give a detailed description of the state of internal stress under such a configuration. Ouwerkerk [4] studied the micromechanical connection between the single-particle strength and the bulk strength of random packing of spherical particles with reference to attrition. They made use of the discrete element method (DEM) to simulate the tests on packed spheres as a function of particle–particle interactions.

Since in a real particulate system the particles will be under multiple contacts we decided to analyze an idealized version of the multiple contact problem. In this paper we describe an analytical method to compute the state of stress in a spherical particle subjected to multiple contact loading on its surface. The method is based on the elasticity solution of Dean, Sneddon and Parsons (DSP solution) [5] for a sphere under a single contact load which is equilibrated by a uniformly dis-

tributed body force. In this paper we have extended the method for spheres under multiple contacts, and the loads are assumed to be self-equilibrating. Numerical results are presented for the case of a sphere under: (i) uniaxial compression; (ii) four-point loading; (iii) three-point in-plane loading; and (iv) six-point orthogonal loading. Interestingly, the maximum tensile stress in the case of three-point in-plane loading is about 25% larger than that in uniaxial compres...on. The stress analysis procedure is also used to study the state of stress in two multiaxial compression tests performed in a companion study [6]. We suggest that the stress analysis will be useful in understanding the breakage of spheres under multiaxial loading.

2. Analytical method

The analysis of stress distribution in a sphere subjected to uniform hydrostatic pressure (pressure normal to the surface of the sphere) on a part of its surface while being decelerated by a uniform body force (Fig. 1) was first studied by Dean et al. [5] in 1944. The stress field obtained by them can be considered as a first approximation to a sphere impacting a target. The static equilibrium was achieved by balancing the external pressure by uniformly distributed body pressure. In this method the applied surface pressure was expanded in a series containing spherical harmonics. A closed-form solution for displacements and stresses was obtained for each term in the series. The solution for each harmonic was then summed to obtain the solution for the stated problem. The stresses are given in a spherical coordinate system shown in Fig. 2. Since the case is an axisymmetric one, out of the six stresses σ_{rr}, $\sigma_{\theta\theta}$, $\sigma_{\phi\phi}$, $\sigma_{\theta\phi}$, $\sigma_{r\phi}$ and $\sigma_{r\theta}$, the two shear stresses with ϕ as one of the subscripts are equal to zero. The formulae for the stresses are given in Appendix A. The stresses are dependent only on the radius of the sphere R, applied pressure μ and the angle θ_0 that defines the contact radius. The solution is in terms of the r and θ coordinates of the point where the stresses need to be found. Because of the axisymmetric nature
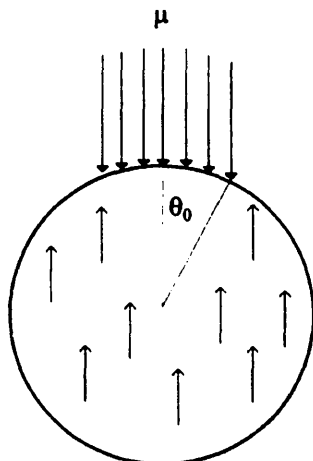

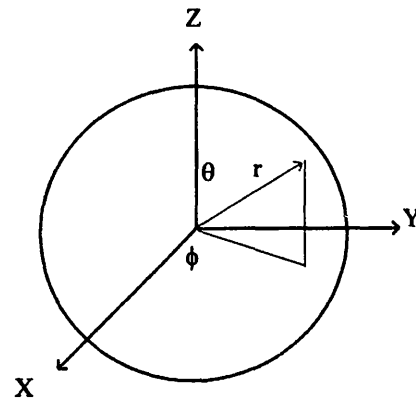Fig. 1. A sphere subjected to uniform pressure and decelerated by a uniform body force.

Fig. 2. Coordinate system for single-particle and multiple particle systems.

of the problem, the solution is independent of ϕ. The accuracy of the solution depends on the number of terms used in the series.

The solution as obtained is linear and hence two or more such solutions can be superposed to obtain solutions for various other problems of practical significance. For example, Shipway and Hutchings [2] superposed two solutions (pressure being applied at $\theta = 0°$ and $\theta = 180°$) to treat the case of a sphere in uniaxial compression. The uniaxial compression case is strictly a contact problem, wherein the contact stress distribution takes an ellipsoidal shape. However, the above solution is fairly accurate as the forces tend to redistribute themselves during compression and hence the assumption of uniform pressure to calculate stresses is valid in this context. Shipway and Hutchings [2] found the stress distribution on the surface of the sphere as well as at points along the loading axis for different contact radii. In their analysis, they found that the maximum tensile stress on the surface occurs at the equatorial belt and this value is about 0.4 times the applied force divided by the maximum cross-sectional area of the sphere. They plotted the maximum tensile stress along the loading axis. They observed that for small c/R, where c is the contact radius and R is the radius of the sphere, the peak tensile stress occurs very near to the surface and that this peak decreases with the increase in c/R and moves toward the center. In the present paper, a similar analysis was carried out for spheres in multi-point compression making use of the DSP solution and subsequent transformation of stresses to a global coordinate system.

In the present study we use the DSP solution [5] to solve the problem of a sphere under multiple contact loading. It is assumed that the external loads are applied in such a way that the sphere is in static equilibrium. The solution to this problem can be obtained by superposing the corresponding DSP solution as the decelerating body forces in the DSP solution [5] will be self-equilibrating and get canceled after the superposition. The superposition procedure is described in Appendix B.

Consider a sphere of radius R under N contact loads acting on the surface. The contact pressures are assumed to be uniform within the respective contact regions and also to be hydrostatic, as assumed in the DSP solution. This means that

the external pressure acts normal to the surface in the contact region and not parallel to the loading axis. However, for small contact radii, we can assume that the entire pressure loading is parallel to the loading axis. Then the ith contact load P_i can be approximated as $P_i \sim \pi c_i^2 \mu_i$ where c_i and μ_i are the ith contact radius and contact pressure, respectively. The contact radius for each contact load can be estimated by using the Hertz formula [7] or from experiments.

The number of terms used to sum the stresses was about 2000 for all examples in this study. There were small oscillations in the stresses for very small contact regions (Gibbs' effect); however, for most cases the solution converged to a constant value.

3. Numerical results

We applied the analytical method described above to four problems: (i) uniaxial compression; (ii) four-point loading; (iii) three-point in-plane loading; and (iv) six-point multiaxial loading. The purpose of the uniaxial compression case was to provide additional results that were not given by Hutchings and Shipway [2]. For example, the results include the state of internal stresses in the entire sphere under uniaxial compression. Cases (ii)–(iv) represent more realistic situations, such as occur in granular flows. In the case of four-point loading (see Fig. 3) the sphere is supported by three identical spheres at the bottom and loaded on the top. Experiments were also conducted on several brittle materials in simulating this configuration. In the case of three-point in-plane loading, the three forces are on one plane and symmetric about the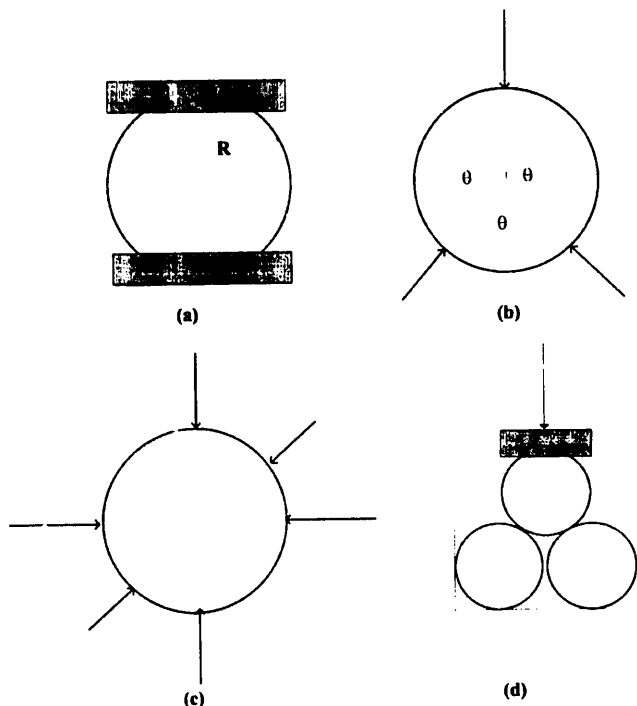 center. In the case of six-point loading, equal and opposite forces are applied along the three mutually perpendicular coordinate axes. These configurations are depicted in Fig. 3. In all cases we limited the value of c/R to 0.2, which is the maximum we observed in the tests conducted in a companion study [6]. All stresses are nondimensionalized with respect to $P_1 / \pi R^2$, where P_1 is the primary load acting on the top of the sphere.

3.1. Uniaxial compression

The maximum tensile principal stresses at points inside the sphere are plotted for $c/R = 0.1$ in Fig. 4. The nondimensional stresses are plotted as a function of r/R for various values of θ. The very high stresses that occur outside the contact circle on the surface of the sphere are not shown in the figure. From Fig. 4 it may be noted that a large volume of the sphere ($0 < r/R < 0.6$, $0 < \theta < 90°$) is subjected to a nondimensional stress of about 0.6. This was the case for $c/R = 0.2$ also. This high value of tensile stress could cause catastrophic failure in spheres where the surface flaws have been removed by some processes such as acid etching or surface erosion.

3.2. Four-point loading

The maximum principal stresses on the surface for $c/R = 0.2$ and for various ϕ values are plotted in Fig. 5 as a function of θ. It must be noted that for this loading the bottom supports are at $\theta = 144.76°$ and at $\phi = 0°$, 120° and 240°, respectively. As is evident from the figure, the stress is very high just outside the contact circles, but it occurs over a narrow region. Elsewhere on the surface the stress is very low and the maximum value of this nondimensional stress is about 0.4, which is the same as that which occurs in uniaxial compression, as discussed in Section 3.1. Further, the surface stresses exhibit good axisymmetry about the loading axis up to $\theta = 100°$. This stress is present over a large volume of the sphere. It was observed that the peak tensile stress near the contact region decreases with increase in c/R, whereas the
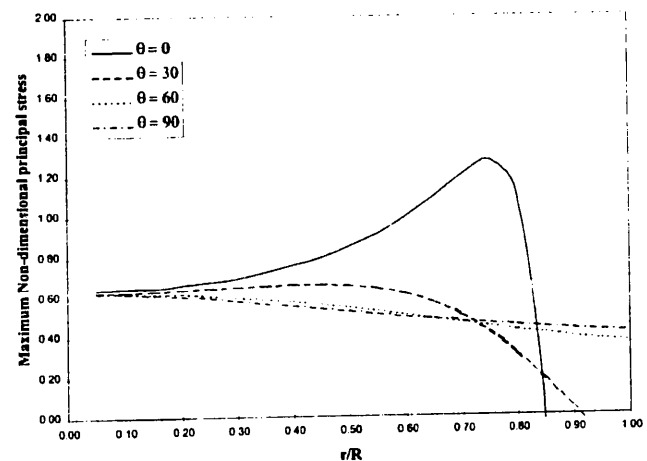

Fig. 3. Different types of loading: (a) uniaxial; (b) three-point in-plane loading; (c) six-point loading; and (d) four-point loading.

Fig. 4. Maximum principal stress along the loading axis in uniaxial compression ($c/R = 0.1$).
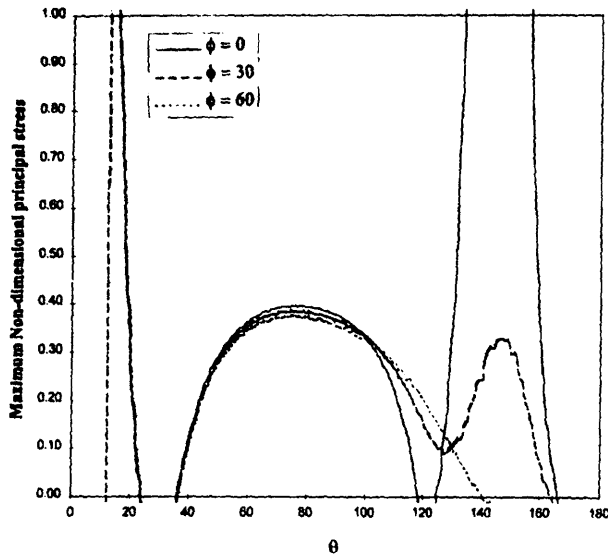
Fig. 5. Maximum principal stress on the surface of the sphere on different planes in four-point tests.
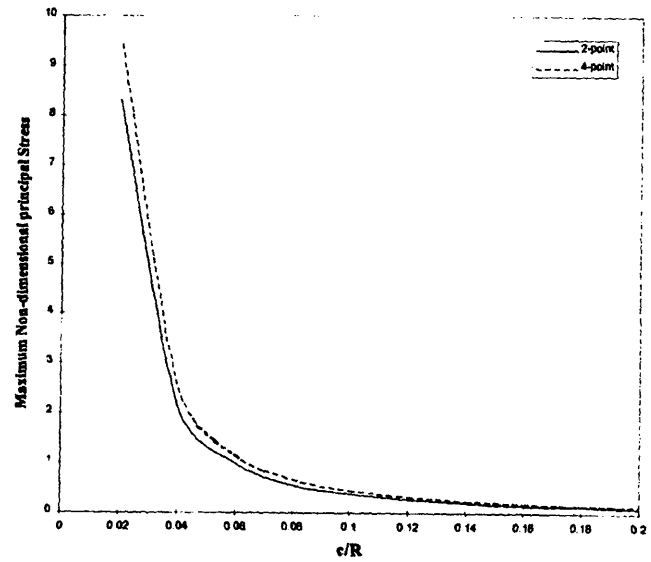

Fig. 7. Maximum principal stress along the loading axis in two-point loading and four-point loading.
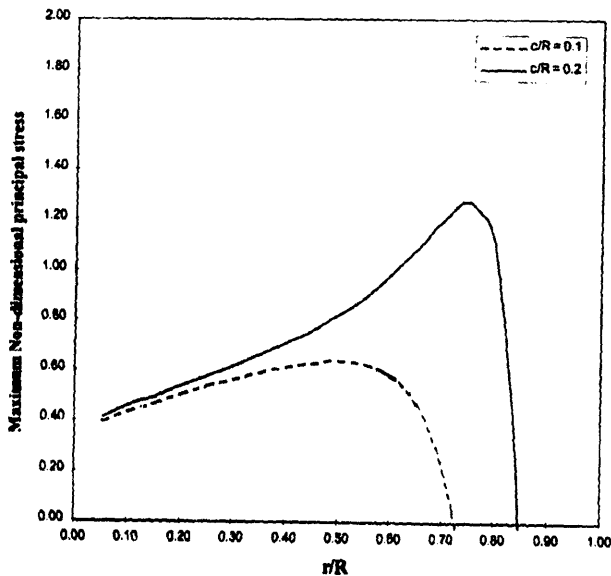

Fig. 6. Maximum principal stress along the loading axis in four-point loading.

Fig. 8. Maximum principal stress along radial lines in the four-point test on the plane defined by $\phi = 0^\circ$ and for $c/R = 0.1$.

maximum stress away from the contact region (~0.4) remains unaffected.

The maximum stress at internal points in the entire top half of the sphere for the case $c/R = 0.1$ can be visualized from Figs. 6–8. The nondimensional principal stresses on the loading axis for $c/R = 0.1$ and 0.2 are shown in Fig. 6. It is clear from these figures that with increase in c/R the peak tensile stress decreases and it also moves closer to the center of the sphere. The maximum internal stress on the loading axis for various c/R values is compared with corresponding results from two-point compression in Fig. 7. It may be noted that the results are identical, indicating that the nature of the bottom supports (either one support or three supports) does not alter the maximum stress that occurs closer to the top contact region, at least for $0 < c/R < 0.2$.

Fig. 8 represents a plot of internal stress against r/R for $\phi = 0$. It may be interesting to compare these figures with the
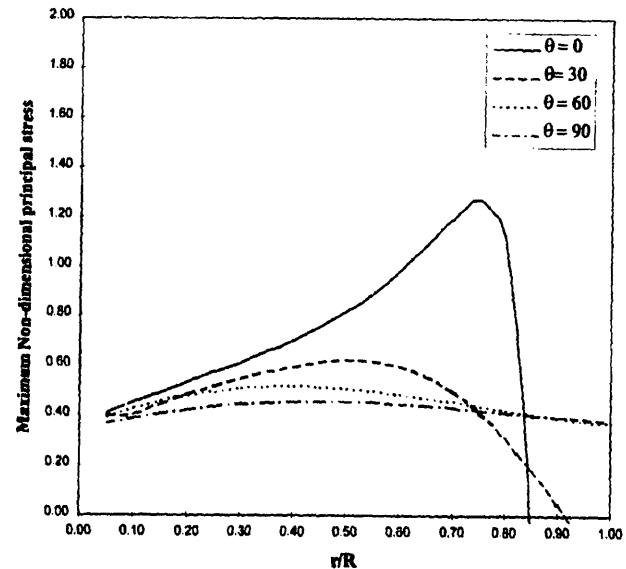
corresponding uniaxial compression results presented in Fig. 4. The maximum stress at the center of the sphere in four-point loading is about 0.4, compared with the value of 0.6 in uniaxial compression. When the internal stress was plotted against r/R for $\phi = 30^\circ$ and 60°, the pattern obtained was similar to that for $\phi = 0^\circ$. The axisymmetric nature of the stresses is approximately preserved for $0^\circ < \theta < 60^\circ$. For $\theta = 90^\circ$ (equatorial plane) the stresses also vary with respect to ϕ. In general, the internal stresses are considerably less in four-point compression than in two-point compression.

3.3. Three-point in-plane loading

In the case of three-point loading, three equal loads were applied in the radial direction on a plane given by $\phi = 0^\circ$
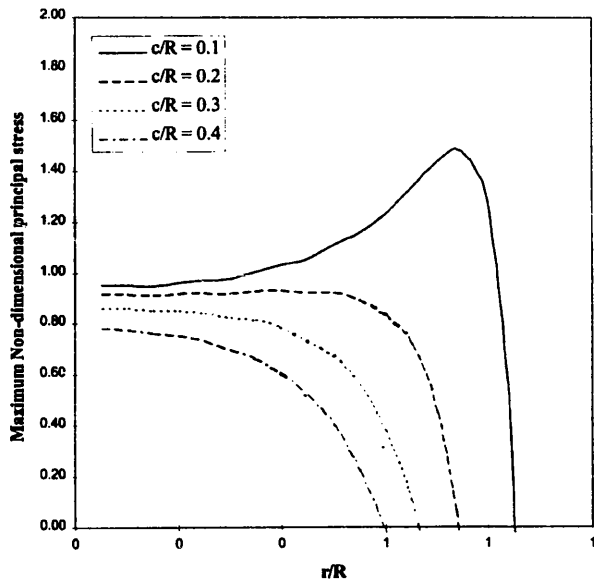
Fig. 9. Maximum principal stress along the loading axis in three-point in-plane loading.
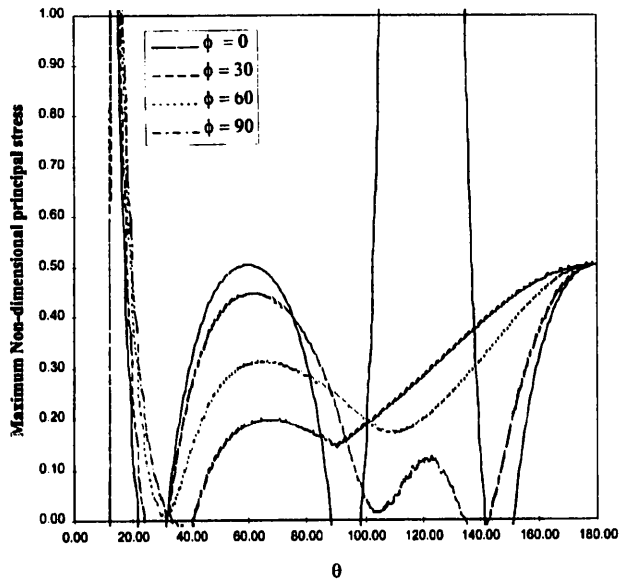

Fig. 11. Maximum principal stress along radial lines in three-point in-plane loading.

Fig. 10. Maximum principal stress on the sphere in three-point loading.
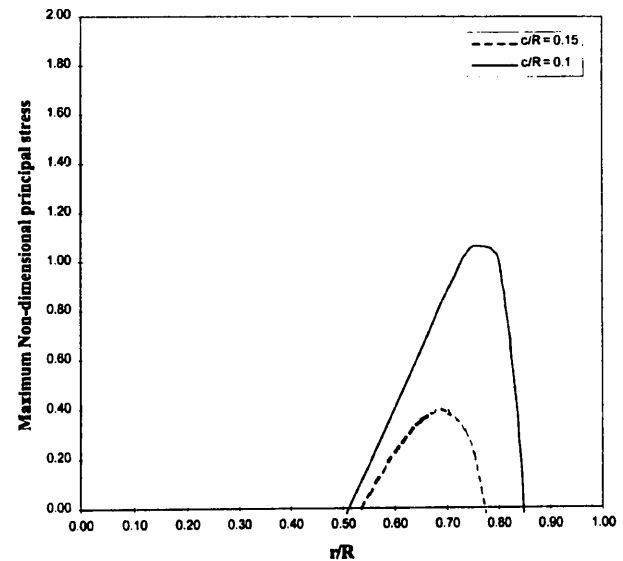
Fig. 12. Maximum principal stress along the loading axis in the six-point test.

(Fig. 3). The (ϕ, θ) values in degrees for the three contact points were (0, 0), (0, 120) and (180, 120), respectively.

Fig. 9 shows the plot of the nondimensional maximum principal stress along the loading axis for $c/R = 0.1, 0.2, 0.3$ and 0.4. It may be noted that very close to the loading point ($r/R = 1$) the stress distribution is similar to that in uniaxial compression. It is observed that the nondimensional stresses in the central region of the sphere are very high (~ 0.9), unlike the cases for uniaxial compression or four-point loading where the corresponding values were 0.6 and 0.4, respectively. The surface stresses for different θ and ϕ values are shown in Fig. 10. It is very interesting to note that the maximum surface stress at regions away from the contact point is about 0.5, which is higher than for the earlier cases where the stress was about 0.4. This maximum stress occurs at $\theta = 60°$ in the loading plane and also at the bottom of the sphere
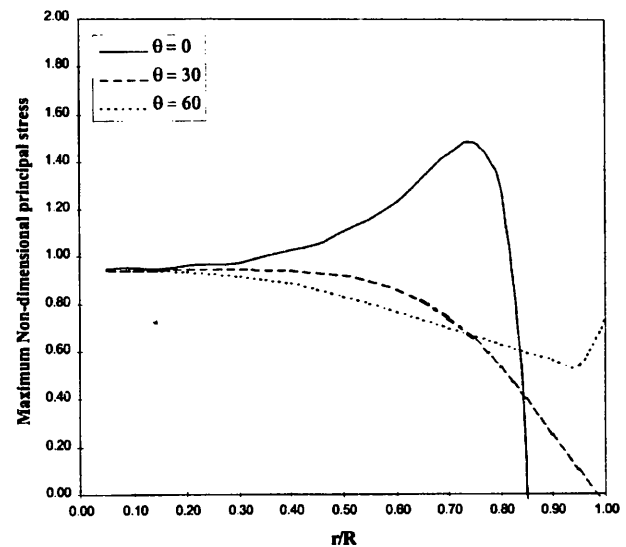
($\theta = 180°$). The stress was also plotted along the radial lines in the loading plane for different θ in Fig. 11. Again it can be seen that the maximum stress is about 0.9 and that it occurs in most of the interior region of the sphere.

3.4. Six-point orthogonal loading

The variation of nondimensional stress along the loading axis for different c/R values is shown in Fig. 12. When compared with uniaxial compression and other types of loading discussed earlier, it may be seen that the region of tensile stress is very limited, and most of the inner region is under compression. Fig. 13 shows the variation of surface stress with θ for different planes (ϕ). The maximum peak tensile stress at points away from the contact region is only 0.2 and it occurs at $\theta = 45°$. The maximum stress away from the
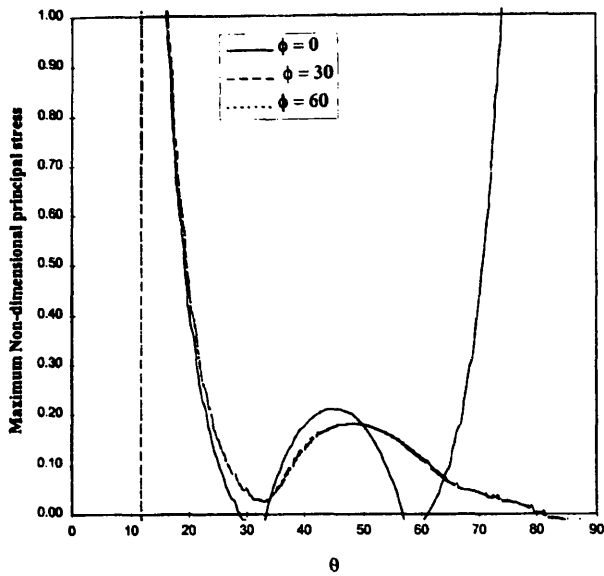
Fig. 13. Maximum principal stress in the six-point test on different planes.

contact region is low and is about 0.2, much lower than that for uniaxial compression.

4. Experimental results

In order to understand better the failure of a spherical particle under multiaxial loading, three types of confined compression tests were performed. In these tests sodalime glass and alumina spheres were subjected to two- and four-

point loading (see Fig. 14). The glass and the alumina spheres were of diameters 3 and 7.94 mm, respectively. In the case of four-point loading the supporting spheres were inside a steel cylinder to prevent lateral movement. The load was applied to the specimens either by a silicon nitride plate or a 9.88 mm diameter silicon nitride sphere. The tests were carried out in an Instron machine at a rate of 25 mm/min until they fractured catastrophically. The broken pieces were carefully collected for use in a fractographic analysis. The origin of fracture was noted in over 80% of the samples for each case. Local failure in the form of chipping in the contact region always occurred at very low loads. Nevertheless, they did not cause any global fracture. More experimental details and results of fractographic analysis are presented in Ref. [6]. In this paper, we will focus on the stress distribution in the spheres and their relation to the nature of fracture.

The material properties that were used in the data reduction are listed in Table 1. The average failure loads from six to eight tests for each case are presented in Table 2 for glass spheres and in Table 3 for alumina spheres. Also presented are the maximum Hertzian contact stresses ($1.5F/\pi c^2$) corresponding to the failure load F, where c is the Hertzian contact radius [7]. Note that in the case of four-point loading the contact stresses were computed either at the top contact point or at the bottom contact points, depending on where the failure was initiated. The next column in Table 2 (also in Table 3) contains the maximum principal stress on the surface computed using the analytical method described in the previous sections. The maximum tensile stress on the loading axis under the top contact point (or above the bottom contact

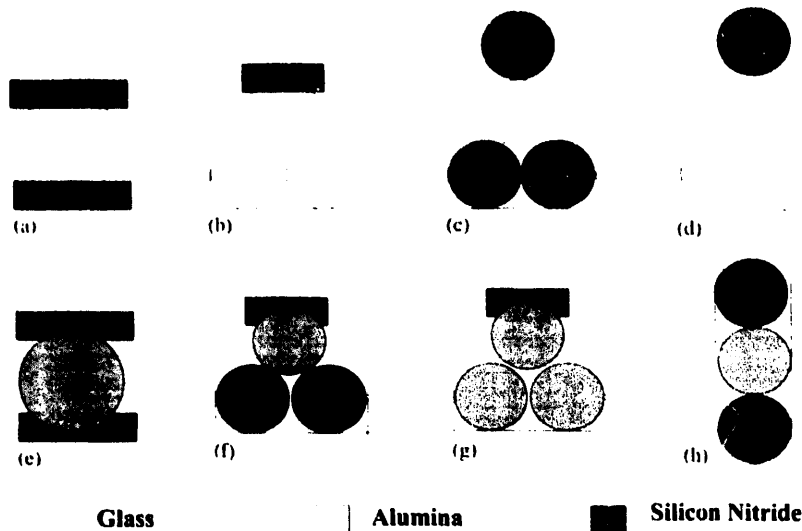Fig. 14. Experimental configuration for the four-point test. Both flat and spherical indentors were used for compression.

Table 1
Material properties for sodalime glass and alumina

Material	Young's modulus (GPa)	Failure strength (GPa)	Fracture toughness (MPa m$^{1/2}$)	Poisson's ratio
Sodalime glass	73	3.6	0.7–0.8	0.25
Alumina	300	5	3–5	0.27

Table 2
Summary of different stresses for glass spheres

Case	Failure load (N)	Type of stress		Axial stress for various values of c/c_H (MPa)					
		Contact stress (GPa)	Surface stress (MPa)	$c/c_H = 1.0$	$c/c_H = 1.1$	$c/c_H = 1.2$	$c/c_H = 1.3$	$c/c_H = 1.4$	$c/c_H = 1.5$
Test A	1110	4.94	63.00	113	105	98	92.3	86.4	82
Test B	870	4.50	61.25	96	87	83	78	76	75
Test C	610	4.00	43.75	77	71	67	63	59	56
Test D	540	4.50	38.75	71	65	61	57	54	51

Table 3
Summary of different stresses for alumina spheres

Case	Failure load (N)	Type of stress		Axial stress for various values of c/c_H (MPa)					
		Contact stress (GPa)	Surface stress (MPa)	$c/c_H = 1.0$	$c/c_H = 1.1$	$c/c_H = 1.2$	$c/c_H = 1.3$	$c/c_H = 1.4$	$c/c_H = 1.5$
Test A	5603	8.73	44.60	115	106.5	99.4	93.3	88	83.4
Test B	6003	10.10	60.00	180	167	156.4	147.3	138.5	131
Test C	6018	11.65	60.00	190	178	165.3	156	146.4	139.2
Test D	4305	12.00	34.30	110	103	89.5	91	85.3	79

point if the failure initiated at the bottom) was also computed. As mentioned earlier, there is local failure under the contact area even for small loading and it might have changed the contact radius and hence the contact stress distribution. Since the maximum stress in the axis is very sensitive to the contact radius, the axis stress was computed for various contact radii varying from 1.0 to 1.5 times the Hertzian contact radius ($c/c_H = 1.0$–1.5). These results are presented in the last six columns of Tables 2 and 3.

The results presented in Tables 2 and 3 were analyzed to find out what stress could have caused the fracture of the spheres. Since the failure was observed to be initiated always in the vicinity of contact, we can conjecture that the failure was due to the stresses on the axis in the vicinity of contact (last six columns in Tables 2 and 3). However, we find that there is no uniformity in these stresses. The variation between various tests is quite significant.

On the other hand, the maximum contact stresses seem to have less variation. Recently, Korsunsky et al. [8] have proposed that fracture of spheres due to impact or static contact can initiate from surface cracks just outside the contact region, and the maximum value of contact stresses plays a significant role in the stress intensity factors of the surface cracks. Thus, we can surmise that for a given flaw distribution the maximum contact stresses can determine the fracture load of the spheres. The exact relation between the fracture toughness and the contact stresses will depend on the flaw size distribution and their location with respect to contact. This will be investigated in detail in a future study.

5. Conclusions

An analytical method has been developed to determine the state of three-dimensional stress in a sphere subjected to mul-

tiple contact loads. The method has been used to study the stress distribution in a sphere under a variety of loading conditions important to particulate systems. It is found that in the case of three-point in-plane loading the maximum tensile stresses are larger than in uniaxial compression. As the number of contact points increases, the maximum internal tensile stress, in general, decreases as the state of stress approaches hydrostatic compression. The method was used to analyze the stresses in some tests carried out on glass and alumina spheres. The stress analysis indicates the maximum contact stress and hence the tensile stress outside the contact circle correlates well with failure and may be responsible for fracture initiation.

Acknowledgements

Appendix A

A spherical coordinate system is used for calculation purposes as shown in Fig. A-1.

Due to the axisymmetric nature of the problem, the two shear stresses with ϕ as one of the subscripts are equal to zero, i.e. $\sigma_{r\phi} = \sigma_{\theta\phi} = 0$. The other stresses are given by the following expressions of the DSP solution [5], where a is the radius of the sphere:
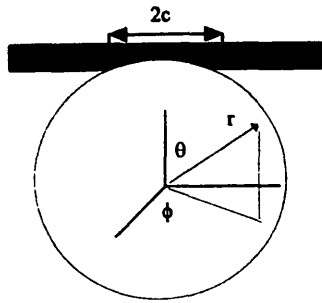
Fig. A-1. Coordinate system for the analytical solution.

$$\frac{\sigma_{r\theta}}{\mu} = -f_0 - f_1\left(\frac{r}{a}\right)\cos\theta - \sum_2^\infty \frac{f_n P_n(\cos\theta)}{4n^2 + 6n + 5}\left(\frac{r}{a}\right)^{n-2}$$

$$\times\left[n(2n^2 + 4n - 1) - (n + 1)(2n^2 - 2n - 5)\left(\frac{r}{a}\right)^2\right]$$

$$(A-1)$$

$$\frac{\sigma_{r\theta}}{\mu} = -\left(1 - \frac{a^2}{r^2}\right)\operatorname{cosec}\theta \sum_2^\infty \frac{n(n+1)(2n^2 + 4n - 1)f_n}{(2n+1)(4n^2 + 6n + 5)}$$

$$\times\left(\frac{r}{a}\right)^n [P_{n-1}(\cos\theta) - P_{n+1}(\cos\theta)] \qquad (A-2)$$

$$\frac{\sigma_{\phi\phi}}{\mu} = -f_0 - f_1\left(\frac{r}{a}\right)\cos\theta$$

$$-\sum_2^\infty \frac{(2n^2 + 13n + 5)f_n}{4n^2 + 6n + 5}\left(\frac{r}{a}\right)^2 P_n(\cos\theta)$$

$$+ \operatorname{cosec}^2\theta \sum_2^\infty \frac{nf_n}{(2n-1)(4n^2 + 6n + 5)}\left(\frac{r}{a}\right)^{n-2}$$

$$\times\left[2n^2 + 4n - 1 - (n-1)(2n+8)\left(\frac{r}{a}\right)^2\right]$$

$$\times [P_{n-2}(\cos\theta) - P_n(\cos\theta)] \qquad (A-3)$$

$$\frac{\sigma_{rr} + \sigma_{\theta\theta} + \sigma_{\phi\phi}}{\mu} = -3f_0 - 3f_1\left(\frac{r}{a}\right)\cos\theta$$

$$-5\sum_2^\infty \frac{(n+1)(2n+3)f_n}{4n^2 + 6n + 5}\left(\frac{r}{a}\right)^n P_n(\cos\theta)$$

$$(A-4)$$

where P_{n+1} is the Legendre polynomial of $(n+1)$th order given by

$$P_{n+1}(\cos\theta) = \frac{(2n+1)\cos\theta P_n(\cos\theta) - nP_{n-1}(\cos\theta)}{n+1}$$

$$(A-5)$$

$$f(\theta) = \sum_0^\infty f_n P_n(\cos\theta) = \begin{cases} 1 & 0 \le \theta \le \alpha \\ 0 & \alpha \le \theta \le \pi \end{cases} \qquad (A-6)$$

then

$$f_0 = \frac{1}{2}(1 - \cos\alpha) \qquad (A-7)$$

and

$$f_n = \frac{1}{2}[P_{n-1}(\cos\alpha) - P_{n+1}(\cos\alpha)] \qquad n \ge 1 \qquad (A-8)$$

Appendix B

Consider a sphere of radius R subjected to a normal surface pressure μ at point $C(X_c, Y_c, Z_c)$, where (XYZ) and $(R\Theta\Phi)$ are the global coordinate systems (Fig. A-2). The pressure is assumed to be uniformly distributed over a contact circle of radius c with C as its center. The state of stress at any point in the sphere can be obtained from the DSP expressions [5]. In this solution, the stresses are referred to the local coordinate system $(r\theta\phi)$. Also, (xyz) represents the local coordinate system within the rectangular coordinate system, where the z-axis passes through the point C and the x-axis is perpendicular to plane AOC and passes through O$(0, 0, 0)$. Apart from the local and global coordinate systems, we define an intermediate rectangular coordinate system, $x^*y^*z^*$. The x^*-axis coincides with the local x-axis and the z^*-axis coincides with the global Z-axis.

In this section we describe the transformation matrices to transfer the stresses from the local coordinates to a global coordinate system, $(R\Theta\Phi)$ or (XYZ). The purpose of the transformation is to express the stresses due to contact loads at different surface points in a common global coordinate system.

In the present problem, the state of stress due to a uniform pressure centered around C is given by the DSP solution [5] in the local $(r\theta\phi)$ coordinate system as $\{\sigma_r\}$. The stress in the local (xyz) coordinate system is given by $\{\sigma_x\}$, and the stresses in global coordinates are given by $\{\sigma_X\}$ and $\{\sigma_R\}$ in the global (XYZ) and $(R\Theta\Phi)$ systems, respectively. It is required to express $\{\sigma_r\}$ in the global $(R\Theta\Phi)$ system. The transformation from the global (XYZ) to the local (xyz) system is carried out via an intermediate rectangular coordinate system given by $x^*y^*z^*$. The main loading axis is the global Z-axis passing through O$(0, 0, 0)$ and A$(0, 0, R)$.

The angle between the vectors $\hat{k}$ and $X_c\hat{i} + Y_c\hat{j} + Z_c\hat{j}$ is given by

$$\cos\theta_1 = \frac{\hat{k}\cdot(X_c\hat{i} + Y_c\hat{j} + Z_c\hat{k})}{(X_c^2 + Y_c^2 + Z_c^2)^{1/2}} = \frac{Z_c}{R} \qquad (B-1)$$
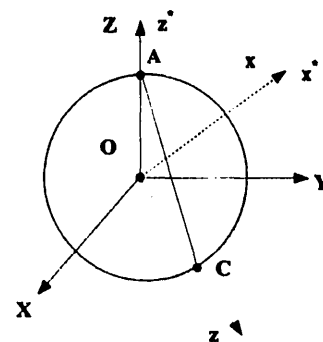

Fig. A-2. The different coordinate systems used in transformation of stresses.

The transformation matrix required to transform the global (XYZ) to the $(x^*y^*z^*)$ coordinate system is given by

$$[T_1] = \begin{bmatrix} -Y_c/R_1 & X_c/R_1 & 0 \\ -X_c/R_1 & -Y_c/R_1 & 0 \\ 0 & 0 & 1 \end{bmatrix}$$ (B-2)

where

$$R_1 = X_c^2 + Y_c^2$$

Also, the transformation needed to rotate the $(x^*y^*z^*)$ coordinate system to the local (xyz) about the x^*-axis is given by

$$[T_2] = \begin{bmatrix} 1 & 0 & 0 \\ 0 & \cos\theta_1 & \sin\theta_1 \\ 0 & -\sin\theta_1 & \cos\theta_1 \end{bmatrix}$$ (B-3)

Hence, the transformation required to transform the global (XYZ) to the local (xyz) is given by

$$[T_3] = [T_2][T_1]$$

$$= \begin{bmatrix} -Y_c/R_1 & X_c/R_1 & 0 \\ -X_c\cos\theta_1/R_1 & -Y_c\cos\theta_1/R_1 & \sin\theta_1 \\ X_c/R_1 & Y_c\sin\theta_1/R_1 & \cos\theta_1 \end{bmatrix}$$ (B-4)

Let

$$[T_3]^{-1} = [T_3]^T = [T_4]$$ (B-5)

The transformation required to convert a vector in the spherical coordinate system $(r\theta\phi)$ to a vector in the rectangular coordinate system (xyz) is given by

$$[T_5] = \begin{bmatrix} \sin\theta\cos\phi & \cos\theta\cos\phi & -\sin\phi \\ \sin\theta\sin\phi & \cos\theta\cos\phi & \cos\phi \\ \cos\theta & -\sin\theta & 0 \end{bmatrix}$$ (B-6)

where

$$\theta = \arccos\left(\frac{Z}{R}\right) \quad \text{and} \quad \phi = \arctan\left(\frac{Y}{X}\right)$$

and the transformation matrix required to transform from the rectangular coordinate system (XYZ) to the spherical coordinate system $(R\Theta\Phi)$ is given by

$$[T_6]$$

$$= \begin{bmatrix} \sin\Theta\cos\Phi & \sin\Theta\sin\Phi & \cos\Theta \\ \cos\Theta\cos\Phi & \cos\Theta\sin\Phi & -\sin\Theta \\ -\sin\Phi & \cos\Phi & 0 \end{bmatrix}$$ (B-7)

where

$$\Theta = \arccos\left(\frac{Z}{R}\right) \quad \text{and} \quad \Phi = \arctan\left(\frac{Y}{X}\right)$$

Hence, the following steps represent the sequential transformation:

$$[\sigma_1] = [T_5]^T\{\sigma_r\}[T_5]$$ (B-8)

$$[\sigma_X] = [T_4]^T\{\sigma_1\}[T_4]$$ (B-9)

$$[\sigma_R] = [T_6]^T\{\sigma_X\}[T_6]$$ (B-10)

and therefore, from Eqs. (B-8), (B-9) and (B-10), we get

$$[\sigma_R] = [T_5]^T[T_4]^T[T_6]^T\{\sigma_r\}[T_6][T_4][T_5]$$ (B-11)

$$[\sigma_R] = \{[T_6][T_4][T_5]\}^T\{\sigma_r\}[T_6][T_4][T_5]$$ (B-12)

References

[1] C.R. Bemrose and J. Bridgewater, Powder Technol., 49 (1987) 97–126.
[2] P.H. Shipway and I.M. Hutchings, Phil. Mag. A, 67 (1993) 1389–1404.
[3] R. Kienzler and W. Schmitt, Powder Technol., 61 (1990) 29–38.
[4] C.E.D. Ouwerkerk, Powder Technol., 65 (1991) 125–138.
[5] W.R. Dean, I.M. Sneddon and H.W. Parsons, Selected Government Research Reports: Strength and Testing of Materials: Part II: Testing Methods and Test Results, H.M.S.O., London, 1952, pp. 212–234.
[6] D.C. Clupper, J.J. Mecholsky, Jr., B.V. Sankar and M. Gundepudi, in N.A. Fleck and A.C.F. Cocks (eds.), Mechanics of Granular and Porous Materials, Kluwer, Dordrecht, 1997, pp. 325–334.
[7] S.P. Timoshenko and J.N. Goodier, Theory of Elasticity, McGraw-Hill, New York, 3rd edn., 1970.
[8] A. Korsunsky, P.D. Warren and D.A. Hills, Wear, 186–187 (1995) 99–104.